ANNALS OF GEOPHYSICS, 69, 2026; doi:10.4401/ag-9332
OPEN ACCESS

Reproducing the Ionosphere Climatology with Different 2D Models

Tamara Gulyaeva[*,1], Valentin Shubin[1]

[(1)] Pushkov Institute of Terrestrial Magnetism, Ionosphere and Radiowave Propagation, Russian Academy of Sciences, Moscow, Russia

Article history: received March 13, 2025; accepted February 25, 2026

Abstract

The first global maps of the F2 layer critical frequency (*foF2*) and the maximum usable frequency factor *M(3000)F2* had been produced in 1960's and approved by the International Telecommunication Union, ITU-R(CCIR). The CCIR maps are used in conjunction with the International Reference Ionosphere, IRI, and the Ionosphere-Plasmasphere, IRI-Plas, model to reproduce *foF2*, *hmF2*, 3D spatial structure of the ionosphere and the total electron content, *TEC*. The more recent global GMF2 model of *foF2* and *hmF2* is for the first time examined in the present study in conjunction with IRI-Plas system for the median prediction of *foF2m*, *hmF2m,* the electron density height profile *Ne*(*h*) and global grids GIM-TEC of *TECm* at altitudes from 65 km to 20000 km (GNSS orbit). Our comparison of IRI-Plas 'model' *TECm* with the 'truth' global UQRG monthly median GIM-TEC for December 2024 showed RMS ≅ 10 TECu. The accuracy of *TECm* could be improved to RMS ≅ 5 TECu by implementing the GTEC model into IRI-Plas yielding the corrected values of *foF2cor, hmF2cor*, *Ne*(*h*)*cor* and *TECcor*. We calculated the 'true' median *foF2* and *hmF2* for quiet geomagnetic conditions (ap < 15 nT) from 45 ionosondes located around the world. Three options of IRI-Plas predictions using CCIR, GMF2 and GMF2cor were compared with the 'true' median *foF2* and *hmF2* from 45 ionosondes located globally for the low solar activity, LSA (2019) and high solar activity, HSA (2024). GMF2 and GMF2cor outperform CCIR at all months of LSA, and in most cases at HSA with the lowest deviation from the reference ionosonde data of *foF2* equal to 8.5% (GMF2) at LSA and HSA, and that of *hmF2* equal to 9.2% (GMF2cor) at LSA and 5.3% (GMF2) at HSA. Data-model comparisons at middle and low latitudes, separated by parallels at ±30° of geomagnetic latitude, shows dominant discrepancies al low latitudes. Since majority of the best results are obtained with GMF2 we recommend the GMF2 *foF2* and *hmF2* to be default options in IRI and IRI-Plas models instead of the CCIR prediction.

Keywords: Global Empirical Model; IRI-Plas; Critical Frequency; Peak Height; Total Electron Content

1. Introduction

The instantaneous maps of the F2 layer peak density and height are in high demand in satellite communication and space based Global Navigation Satellite System (GNSS). Using data of the network of sounding stations available since 1940, the first global maps of the F2 layer critical frequency (*foF2*) and the maximum usable

frequency factor *M*(*3000*)*F2* have been produced in 1960's and approved by the International Telecommunication Union, ITU-R (Jones and Gallet, 1962; CCIR, 1966). The CCIR maps (CCIR, 1966) are used in conjunction with the International Reference Ionosphere, IRI (Bilitza et al., 1979, 2017, 2022, 2024) and the Ionosphere-Plasmasphere, IRI-Plas, model (Gulyaeva and Bilitza, 2012; Gulyaeva et al., 2013) to reproduce *foF2*, *hmF2*, 3D spatial structure of the ionosphere and the total electron content, *TEC*. The IRI also includes the option to use the URSI model for *foF2* (Rush et al., 1989). Since 2016, two different models of *hmF2*, namely, AMTB-2013 model (Altadill et al., 2013) and GMF2 hmF2 model (Shubin, 2015) have been included in IRI (Bilitza et al., 2017, 2022). Efforts are underway to improve the F2 layer climatological models with the more extended database such as NPDM *NmF2*, NPHM *hmF2* (Hoque and Jakowski, 2011, 2014), GMF2 *foF2* and *hmF2* (Shubin, 2015, 2017; Shubin and Deminov, 2019; Shubin and Gulyaeva, 2021) and CLIM2 model of *foF2* and *hmF2* (Edwards et al., 2025a, 2025b).

The International Reference Ionosphere (IRI) model and its extension into the plasmasphere (e.g., IRI-Plas) have been built to represent the monthly average behavior of space plasma accepted as the international standard by COSPAR, URSI and the International Standardization Organization, ISO (Bilitza et al., 2017, 2022, 2024; Bilitza, 2023; Gulyaeva et al., 2013; ISO 16457, 2022). The IRI and IRI-Plas are using the *F2* layer peak parameters from the CCIR maps of the *F2* layer critical frequency (*foF2*) and the maximum usable frequency factor M(3000)F2 converted to the peak height (*hmF2*) (CCIR, 1966; Bilitza et. al., 1979). Both IRI and IRI-Plas have an option to input the measured or instantaneous values of *foF2* and *hmF2* to scale the electron density profile according to the current conditions in the ionosphere. Using any empirical model as a background climatology with assimilation of the real-time observations is very helpful in the operational ionospheric parameter reconstruction. Missing *foF2* and *hmF2* instant data, input of GNSS derived *TEC* between satellite (20 000 km orbit) and ground station is ingested in IRI-Plas to produce instant F2 layer peak parameters and the electron density profile *Ne*(*h*) through the ionosphere and plasmasphere providing continuous global coverage (Gulyaeva et al., 2013).

Nowadays, the Total Electron Content (*TEC*) is one of the most widely used parameters that represent the ionospheric variability in space and time (Hernández-Pajares, 2009). Global ionospheric maps GIM-TEC are used by the assimilative models for their inversion into the instantaneous maps of the F2 layer peak electron density and height because they are the most accessible global characteristics of the ionosphere (Gulyaeva et al., 2013; Gerzen et al., 2015; Galkin et al., 2022). Assessing the effectiveness and uncertainties of assimilative procedures to contemporary global empirical ionospheric models presents challenge for the contemporary models (Gerzen et al., 2015). In particular, it was found that the accuracy of the IRI electron density model based on global ionosonde data in 2011 and 2015 is typically from 15% to 25% at low and middle dip latitudes (<60°) and 50% to 80% at high dip latitudes (>60°) at heights from 200 km to 1 000 km (Arikan et al., 2019; Edwards et al., 2025b; ISO 16457, 2022; and references therein). A global assessment of the accuracy of the characteristics of the ionospheric F2 peak was made using radio occultation RO data co-located with the ionosonde data (McNamara and Thompson, 2015; Ratovsky et al., 2017; Paul et al., 2025). The comprehensive validation by Paul et al. (2025) establishes COSMIC-2 as a reliable source of high-quality data characterizing the peak of the ionospheric electron density.

This paper discusses for the first time the implementation of GMF2 maps of *foF2* and *hmF2* (Shubin, 2015, 2017; Shubin and Gulyaeva, 2021) in conjunction with IRI-Plas code for the monthly median prediction of *foF2m*, *hmF2m, Ne*(*h*) profile and *TECm* at altitudes from 65 km to 20 000 km (GNSS orbit). Adjustment of IRI-Plas *TEC* results obtained with the peak parameters *foF2* and *hmF2* of GMF2 to the global model of the total electron content GTEC (Shubin and Gulyaeva, 2022) produces a new set of corrected IRI-Plas output parameters – *foF2cor, hmF2cor, Ne*(*h*)*cor* profile and *TECcor*. We examine three options of the IRI-Plas implementation of the F2 layer peak and *TEC* parameters: (1) GMF2 denotes *foF2* and *hmF2* from GMF2 model which serve as input in IRI-Plas to produce *TEC*; (2) GMF2cor – *foF2*, *hmF2* input from GMF2 model aligned with GTEC model which are used as input in IRI-Plas to produce *foF2cor*, *hmF2cor* and *TECcor*; (3) CCIR – IRI-Plas calculation of *foF2*, *hmF2* and *TEC* using CCIR coefficients. We compare IRI-Plas results of *TEC* under the different combinations of the F2 layer peak indices with measured GIM-TEC 'truth' data to estimate reliability of IRI-Plas *TEC* predictions. The sequence of CCIR, GMF2 and GMF2cor in IRI-Plas is then compared with the 'truth' ionosonde data of the *foF2* and *hmF2* in order to assess their effectiveness in low solar activity, LSA (2019) and high solar activity, HSA (2024) worldwide. IRI recommends the use of the CCIR model over the continents and the URSI model over the oceans. The ionosonde data used here for comparisons are located on continents, so comparisons are made with the CCIR option. Results are presented in the following Sections.

2. Data Analysis

The International Reference Ionosphere-Plasmasphere (IRI-Plas) code is used in the assimilative mode as the three-dimensional (3D) interpolator of the GNSS-derived total electron content, *TECobs*. The brief diagram of IRI-Plas processing components is plotted in Fig. 1. Similar to IRI, the execution starts specifying the input parameters: year, month, day, universal UT or local LT time of day, geographic or geomagnetic latitude and longitude, and index of solar activity, SA. These parameters serve as drivers of the CCIR *foF2* and *M*(*3000*)*F2* issue which in turn are used to produce the IRI-Plas quiet time parameters, including the peak height *hmF2*, the electron density *Ne*(*h*) height profile, the temperature height profile and the total electron content *TEC*. Extra input of observed or modelled GIM-TEC is envisaged to upgrade GMF2 peak density and height yielding corrected proxies *foF2cor, hmF2cor*, *Ne*(*h*)*cor* and *TECcor*. IRI-Plas is applied for producing electron density *Ne*(*h*)height profile at altitudes from 65 km to 20 000 km (GNSS orbit) crossing the peak of the F2 layer electron density at the peak height minimizing the deviation of the model *TECm* from the instantaneous *TECobs* retrieved from the source GIM-TEC at each grid point of the map.

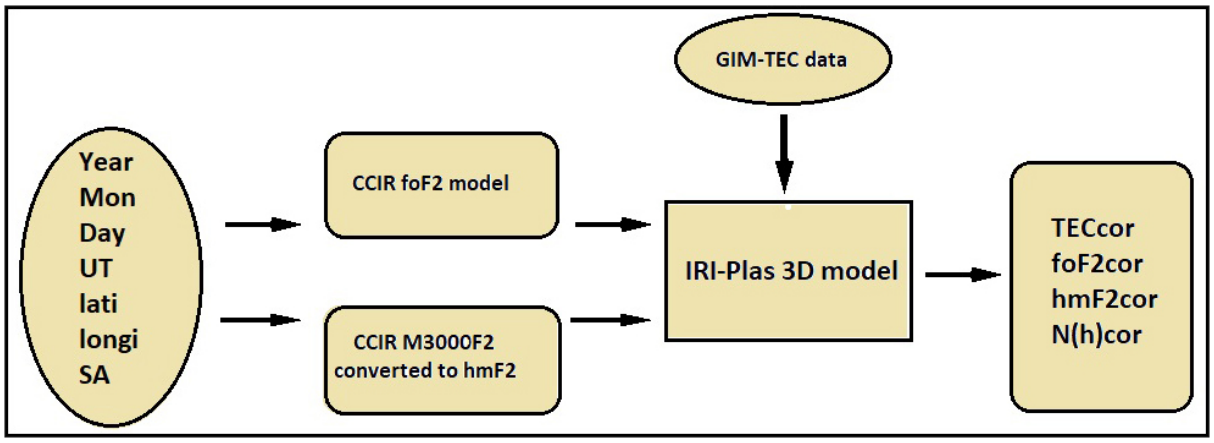

Figure 1. Flowchart of IRI-Plas operation.

The global median GMF2 model is an empirical model of the F2 layer peak parameters (foF2 and hmF2), observed on a global network of 248 ground-based ionospheric stations from 1958 to 2022, as well as ~5 × 106 satellite radio occultation profiles of electron density (ED) for the period from 2001 to 2022. These data allowed for near-global coverage of foF2 and hmF2 in 15° increments in longitude and 5° increments in latitude, corresponding to 864 cells for each month at a fixed UT hour. The global median empirical GTEC model of total electron content as well as GMF2 foF2 and hmF2 models are based on spherical harmonic analysis. The GTEC model is built from the global GIM-TEC ionospheric maps produced by the Jet Propulsion Laboratory, JPL, from 1996 to 2019. The Legendre method is used in developing the GMF2 and GTEC models to spatially decompose the monthly medians foF2, hmF2 and TEC calculated from the relevant database, and then the Fourier method is applied to decompose the resulting coefficients over time UT (Shubin, 2015, 2017; Shubin and Gulyaeva, 2021, 2022). The coefficients of the GMF2 and GTEC models were calculated for use in the IRI-Plas model with a recalibrated 12-month smoothed sunspot number SSN2. Here, we analyse the GMF2 and GTEC models for the quiet median condition to compare them with the median empirical CCIR model.

The valid 'truth' GIM-TEC data for the comparisons with the modelled TECm were obtained from the rapid UQRG GIMs on a 15 min cadence by Polytechnical University of Catalonia, Barcelona, Spain (UPC), gAGE/UPC, which can be downloaded from the FTP server ftp://cddis.gsfc.nasa.gov/gps/products/ionex/ (Hernández-Pajares et al., 2009). JPL 1-hour cadence GIM-TEC and UQRG 15-minute cadence GIMs are analysed daily on the IZMIRAN website (https://www.izmiran.ru/ionosphere/weather/) to obtain GIM-foF2, GIM-hmF2, GIM-W index maps. JPL GIM-TEC were used to build the GTEC model, so we selected UQRG GIM for analysis here. UPC is using a Kriging based interpolation scheme to generate TEC maps. The maps are arranged in IONEX format at latitudes from 87.5°N to 87.5°S in step of 2.5°, longitudes from 180°W to 180°E in step of 5°. The 15-min TEC maps start at 00:00 UT and

end at 23:45 UT but only hourly GIMs are used in the present study. The UPC GIMs are in agreement with the different 'truth' ~ 'truth' data pairs of GIMs (Roma-Dollase et al., 2017). Because of their global nature, these 2D maps are suitable for statistical studies or three-dimensional model products evaluations along with other measurements to make meaningful conclusions on model operation.

We calculated the deviation of the model from the reference 'truth' data from pixel to pixel and epoch to epoch and then estimated the root mean square (RMS) of the differenced values:

$$RMS = \sqrt{\frac{1}{N}\sum_{1}^{N}(Ym - Yo)^2} \tag{1}$$

Here N is the number of data pairs, Ym– model, Yo– empirical value.

The percentage deviation between 'model' prediction and 'truth' data is obtained with Eq. (2):

$$PRMS = \sqrt{\frac{1}{N}\sum_{1}^{N}\left(\frac{Ym - Yo}{Yo}\right)^2} \times 100 \tag{2}$$

To produce the instant proxy *foF2* from the CCIR or GMF2 median *F*2 layer critical frequency (*foF2m*), we assume that the ratio of *NmF2/NmF2m* (equivalent to $foF2^2/foF2m^2$) is zequal to the ratio *TECobs/TECm* so that an instant proxy $foF2 \cong \sqrt{NmF2}$ is obtained from Eq. (3):

$$NmF2 = NmF2m \times TECobs/TECm \tag{3}$$

We need then to generate the instant proxy F2 layer peak height which cannot be straightforward delivered from the instant *TECobs*. A good solution for this purpose presents an empirical model of the instantaneous *hmF2* expressed versus changes of *foF2* derived from the topside sounding database (Gulyaeva, 2012). That model presents anticorrelation of log (*hmF2/hmF2m*) with log (*foF2/foF2m*) in terms of the solar activity SA, season and magnetic latitude Φ:

$$\log\left(\frac{hmF2}{hmF2m}\right) = F\left(\log\left(\frac{foF2}{foF2m}\right), SA, season, \Phi\right) \tag{4}$$

Details of the model (Eq. (4)) are provided in (Gulyaeva, 2012). Denoting $Dlogh = \log(hmF2/hmF2m)$ and $Dlogn = \log(NmF2/NmF2m)$ with $NmF2 \sim foF2^2$, the dependence of *Dlogh* on *Dlogn* is expressed by a linear function: $Dlogh = \alpha + \beta \times Dlogn$ at 8 thresholds of ionospheric perturbation W index, which ranges from –4 (intense negative storm) to +4 (intense positive storm) in increments of 1. After obtaining the median of *Dlogh* and *Dlogn* for the eight specified W-index segments, the least squares approximation is applied to the *NmF2m* and *hmF2m* medians of the topside sounding data in the selected magnetic latitude ranges Φ for three *seasons* and two levels of solar activity *SA* (high solar activity, HSA, and low solar activity, LSA). Such analysis was performed to obtain regression coefficients α and β for the ranges of magnetic latitudes, for specific seasons and solar activity conditions (Gulyaeva, 2012). Procedures for implementation of Eqs. (3) and (4) for the proxy *foF2* and *hmF2* are incorporated in IRI-Plas code which can be retrieved from https://www.izmiran.ru/ionosphere/weather/grif/SPIM/.

Since the CCIR, GMF2 and GTEC models together with IRI-Plas are involved in specifying the median quiet-time conditions, we will compare the results of the *foF2*, *hmF2* and *TEC* models with the 'true' median of GIM-TEC and the 'true' median of the ionosonde data at the network of stations shown in Fig. 2.

The ionosonde data are retrieved from the University of Massachusetts, Lowell, GIRO Digital Ionogram Database at https://giro.uml.edu/didbase/scaled.php. Validation of foF2 and hmF2 is made for the local time 00, 01, …, 23 h LT. We produced the monthly median from the daily-hourly data foF2 and hmF2 for each month during the year of minimum solar activity, LSA (2019) and maximum, HSA (2024). We calculated the 'true' median foF2 and hmF2 for quiet geomagnetic conditions (ap < 15 nT) from 45 ionosondes located around the world, according to the

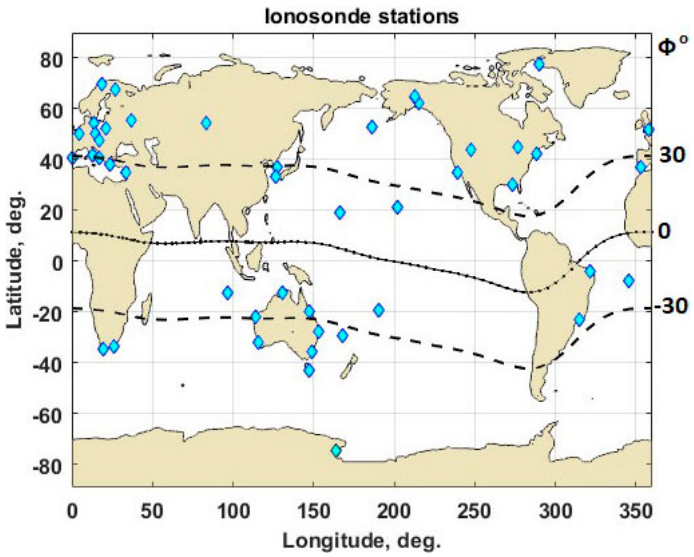

Figure 2. Location of the 45 ionosondes that provided *foF2* and *hmF2* data for IRI-Plas validation.

conditions adopted in the construction of GMF2 models. The geomagnetic dip equator is shown as a solid line in Fig. 2. In addition, the magnetic latitudes $\Phi = \pm 30°$ shown in dashed lines are separating the mid and low latitude regions for which the RMS is calculated. The monthly medians are compared with the model predictions of the quiet time foF2 and hmF2.

We examine the global performance of the F2 layer peak parameters – foF2 and hmF2 – with three implementations of the IRI-Plas peak model of the F2 layer: CCIR, GMF2 and GMF2cor. Comparison of the IRI-PLas 'model' with the 'true' median foF2 and hmF2 from the ionosonde observations is made using Eqs. (1) and (2) for each month at low solar activity, LSA (2019) and high solar activity, HSA (2024). The ionosonde stations in Fig. 2 are distributed throughout the world at different latitudes and longitudes. Therefore, the F2 layer peak parameters for these locations can be used to construct the dependence on latitude and local time LT. The input data and modeling results are also binned in two latitudinal zones – middle and low latitudes separated by geomagnetic latitudes $\Phi = \pm 30°$, and two levels of solar activity – the solar minimum (2019) and maximum (2024). Results of the comparison are provided in the next Section.

3. Results

A realistic 'true' monthly median *TECobs* characterizing quiet time ionosphere plasma behavior is calculated from the UQRG GIM-TEC daily-hourly map set for the selected month. The standard RMS difference between the UQRG *TECobs* and the IRI-Plas GIM *TECm* or GTEC model *TECmod* is examined for each UT hour (Eq. (1), N = 5183 for the GIM pair).

The IRI-Plas mode of operation producing the median *TEC* using CCIR and/or GMF2 model (*foF2* and *hmF2*) and the independent GTEC model are shown in Fig. 3. The RMS deviation from the monthly median 'true' UQRG GIM is calculated using Eq. (1) from 0 to 23 hours UT for December, 2024 (HSA, the recalibrated 12-month smoothed sunspot number $SSN2_{12} = 140$). The IRI-Plas results are plotted for the following selection of the F2 layer peak parameters: (1) CCIR *foF2* and *M(3000)F2* converted to *hmF2* (IRIP-CCIR, cyan), (2) GMF2 *foF2* and *hmF2* (IRIP-GMfh, blue), (3) GMF2 *foF2* and CCIR *M(3000)F2* converted to *hmF2* (IRIP-GMf, red), (4) CCIR *foF2* and GMF2 *hmF2* (IRIP-GMh, green). The deviation of the IRI-Plas (1)-(4) sequence from the'true' GIM-TEC UQRG data shows an RMS in the range 6.5 to 10.5 TECu which exceeds by about a factor of 2 the RMS of *TECmod* for GTEC model, varying in the range 4.6 to 7.0 TECu (GTEC, black, diamond). Note that the GTEC model was built from Jet Propulsion Laboratory, JPL, GIM-TEC database (Shubin and Gulyaeva, 2022), while GTEC is compared here with the median GIM-TEC of UQRG. So, RMS obtained here with GTEC 'model' ~ 'truth' comparison can include both GTEC model errors and the difference between JPL and UPC 'truth' ~ 'truth' data pairs of GIMs It should be noted that the global GTEC model based on JPL GIM-TEC ionospheric maps, as well as UQRG maps, incorporate inherent errors associated

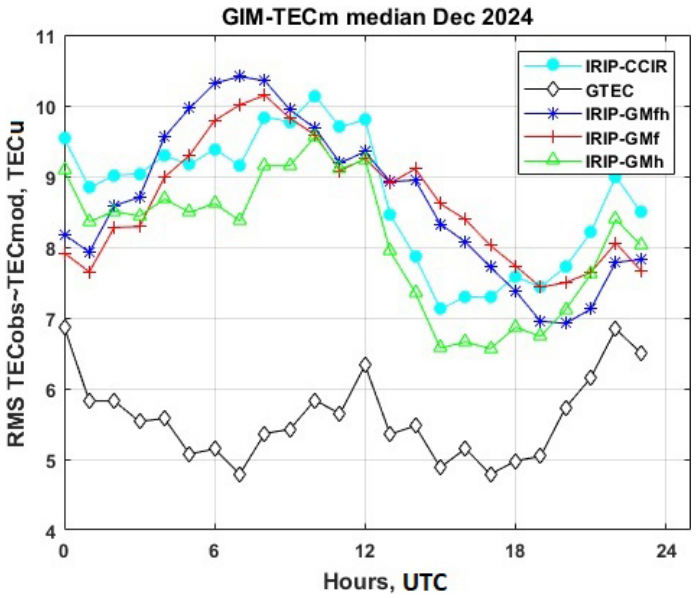

Figure 3. RMS results for different options of the IRI-Plas *TECm* and GTEC model compared with the monthly 'true' median of the UQRG GIM-TEC.

with the mapping process itself, which include the conversion of oblique TEC (STEC) to vertical TEC, the specific mapping and interpolation algorithms used, and the data quality/coverage issues (Hernández-Pajares et al., 2009; Roma-Dollase et al., 2017).

The ability to assimilate GIM-TEC using IRI-Plas technology is illustrated in Fig. 4. Similar to setting the Ne(h) IRI-Plas profile to instant *TEC* (Eqs. 3 and 4), we apply the *TEC* from the GTEC model to update the F2 layer peak parameters with the IRI-Plas model. RMS difference between *TECm* model and UQRG monthly median *TECobs* (Eq. (1),

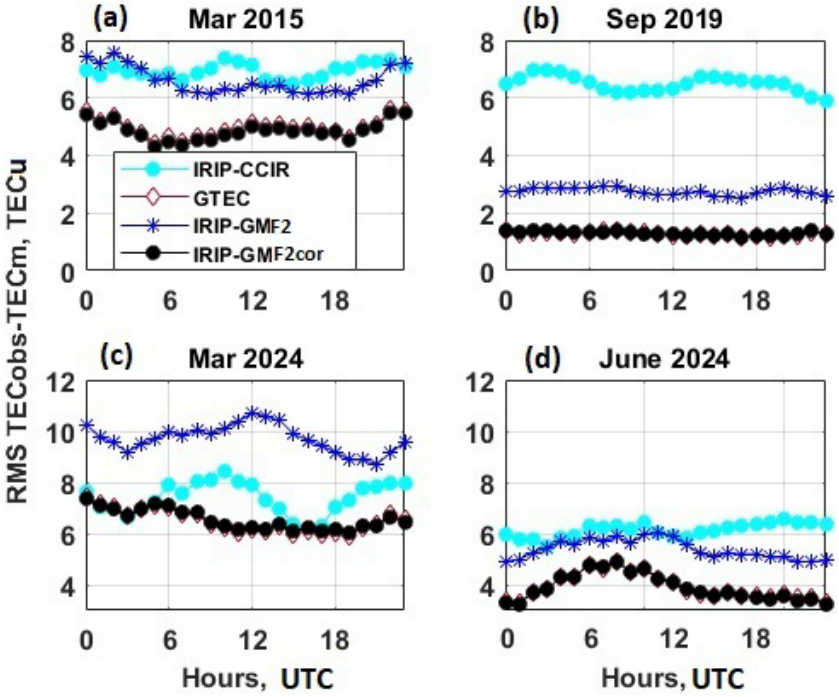

Figure 4. RMS deviation of the CCIR, GMF2 and GMF2cor options of the IRI-Plas *TECm* and GTEC 'model' from the GIM-TEC UQRG 'true' monthly median. (a) March 2015; (b) September 2019; (c) March 2024; (d) June 2024.

N = 5183 for each UT hour) is shown in Fig. 4: (a) March 2015 (HSA, $SSN2_{12} = 82$); (b) September 2019 (LSA, $SSN2_{12} = 3$); (c) March 2024 (HSA, $SSN2_{12} = 141$); (d) September 2024 (HSA, $SSN2_{12} = 144$). As in Fig. 3, the RMS for the median *TECm* from IRI-Plas CCIR in Fig. 4 (IRIP-CCIR, cyan) and IRI-Plas GMF2 (IRIP-GMF2, blue) is greater than the RMS for the GTEC median (GTEC, brown, diamonds) in all cases. The RMS of the GTEC 'model' ~ 'truth' GIM varies from 1.5 TECu (panel (b), LSA) to ~7 TECu (panel (c), HSA). When the median GTEC is assimilated by IRI-Plas (Eqs. (3) and (4)) the synthesized values of *foF2cor*, *hmF2cor* and *TECcor* (IRIP-GMF2cor, black) are obtained. The results of *TECcor* with GTEC adjustment in the IRI-Plas are very close to the original GTEC median (RMS < 1 TECu). Thus, the close alignment of IRI-Plas results with GTEC input data justifies the assumption that the knowledge of the *TEC* variability can predict the approximate variability of *NmF2* (~*foF2*) and *hmF2* (Eqs. (3) and (4)).

The daily variation characteristics of the global median *foF2* and *hmF2* calculated for the two levels of solar activity for the ionosonde collection shown in Fig. 2 are presented in Fig. 5a-b. Here, the 'truth' ionosonde data and the three simulations (CCIR, GMF2 and GMF2cor) of critical frequency (Fig. 5a) and peak height (Fig. 5b) are for December 2024 (HSA, solid curves) and December 2019 (LSA, dotted curves). The diurnal variation of the *foF2* shows an increase in peak plasma density by noon with increasing solar irradiance, while the peak height shows growth by nighttime due to electrodynamical uplift of the ionospheric plasma. The magnitude of both the critical frequency and peak height is greater at the solar maximum than at the solar minimum.

The global distribution of *foF2* critical frequencies is shoen in Fig. 6a-d in the local time LT and latitude ϕ frame. Fig. 6a shows an example of the daily variation in 'true' median *foF2obs* observed by ionosonde for December 2024 (HSA). The CCIR *foF2* in Fig. 6c is constructed in the same way. The GMF2 *foF2* model is shown in Fig. 6b, and GMF2cor proxy *foF2* upgraded with GTEC model (Eq. 3) – in Fig. 6d. All results demonstrate a typical diurnal *foF2* change increasing by noon, and a latitudinal increasing trend towards Equatorial Ionization Anomaly (EIA). The best correspondence to the 'true' data (Fig. 6a) is acheaved by GMF2 model (Fig. 6b). Their quantitative comparisons will be discussed below.

The *hmF2* peak height resultsResults of the peak height *hmF2* are shown in Fig. 7a-d similar to Fig. 6a-d. Thedaily variation of the 'true' median *hmF2obs* observed by the ionosonde for December 2024 (HSA) is shown in Fig. 7a in the latitude ϕ and local time LT frame. Model *hmF2* derived from CCIR *M(3000)F2* maps are shown in Fig. 7c. The GMF2 model *hmF2* is shown in Fig. 7b, and the GMF2cor proxy *hmF2* updated after GTEC assimilation (Eq. 4) shown in Fig. 7d. Unlike *foF2* changes, the daily variation in *hmF2* does not tend to increaseanywhere by noon except for the EIA region. In general, *hmF2* increase by night worldwide with particular increases by dusk and night time

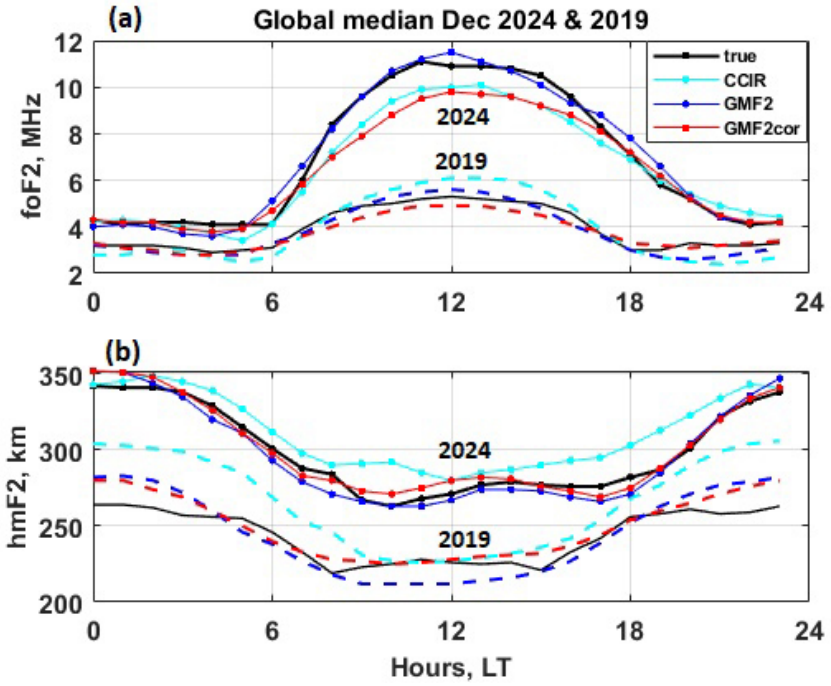

Figure 5. Diurnal variation in global median F2 layer peak parameters at solar minimum (2019) and solar maximum (2024): (a) *foF2*; (b) *hmF2*.

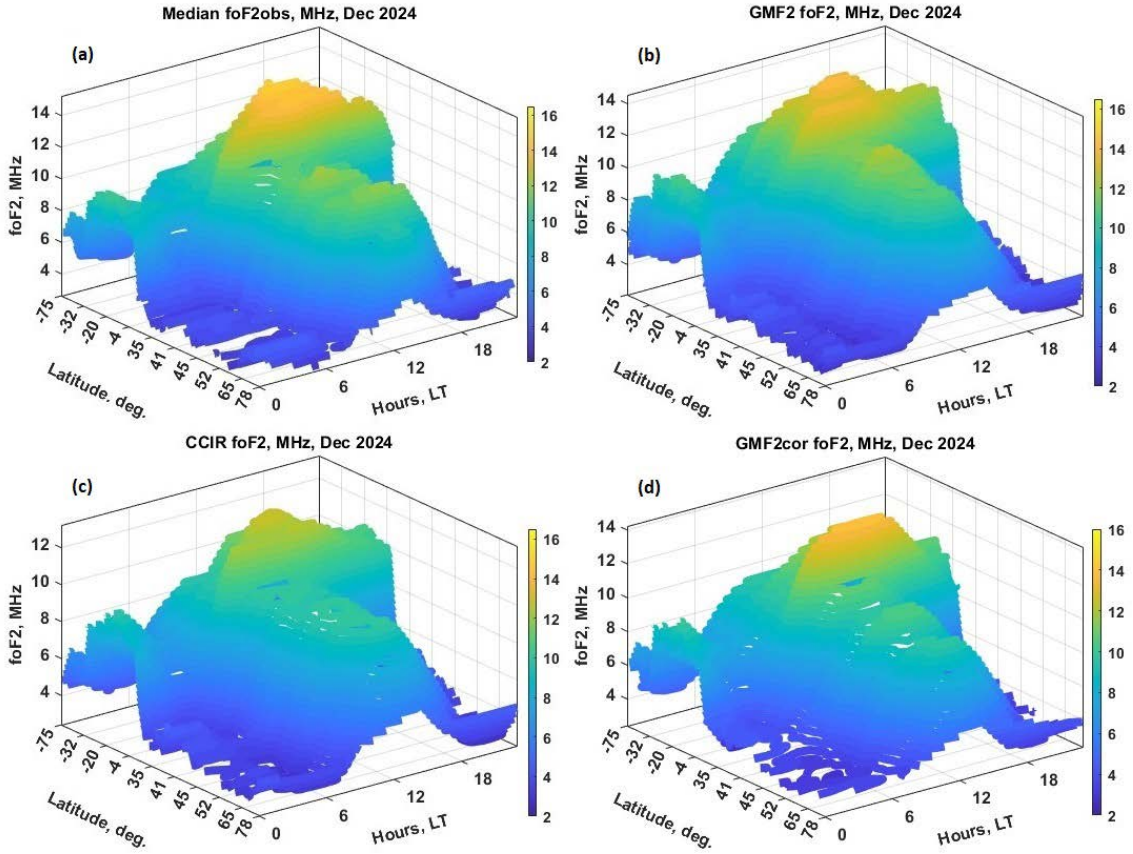

Figure 6. Diurnal – latitudinal variation of the critical frequency *foF2* in December 2024: (a) observed median at 45 ionosonde stations; (b) GMF2 model; (c) CCIR model; (d) GMF2 *foF2cor* model produced by IRI-Plas with GTEC assimilation GTEC (Eq. 3).

near EIA. Again, the better correspondence to the 'true' data (Fig. 7a) is obtained with the GMF2 model (Fig. 7b). RMS quantitative results (Eq. 1) for the data pairs 'truth' ~ 'model' for all months of 2019 (LSA) and 2024 (HSA) are presented in Fig. 8, their percentage deviation PRMS (Eq. 2) in Table 1, and RMS for mid and low latitudes in Fig. 9.

RMS between 'true' median *foF2obs* at 45 selected stations for 24 LT hours each month (Eq. (1), $N = 45 \times 24 = 1080$) and the 'proxy' model *foF2* is shown in Fig. 8a, c (left panels). RMS between 'true' median *hmF2obs* and the 'proxy' *hmF2* is shown in Fig. 8b, d (right panels). The LSA (2019) data is in the lower panels and HSA (2024) data in the upper panel. Results for GMF2 (red), GMF2cor (yellow) and CCIR (cyan) show less RMS at GMF2 or GMF2cor in all cases for LSA, except for a few cases with few cases where CCIR results show less RMS for the F2 layer peak density (critical frequency) and height at HSA. Note that RMS < 0.9 MHz is observed for foF2 at LSA (Fig. 8c) but a larger RMS < 1.5 MHz is obtained at HSA (Fig. 8a), similar to large absolute values of the global median *foF2* (Fig. 5a) at the solar maximum. At the same time, the RMS for *hmF2* varies from 20 to 50 km in magnitude at the both levels of solar activity (Fig. 8b and 8d). Since the absolute values of the *hmF2* increase from the solar minimum to the maximum (Fig. 5b), we will consider the percentage deviation, PRMS (Eq. 2) month-to-month in Table 1.

Table 1 includes monthly PRMS results for the 'true' ~ 'proxy' *foF2* pairs (columns 2-4) and *hmF2* (columns 5-7) for 2024 (HSA) and 2019 (LSA). Minimum PRMS for GMF2, GMF2cor and CCIR are shown in bold on a yellow background. GMF2 surpass CCIR for all months at a solar minimum (2019) in both *foF2* and *hmF2* characteristics. GMF2 and GMF2cor outperform CCIR during most months of the solar maximum (2024), but there are PRMS minima with CCIR for *foF2* in April and May 2024, and in July and August 2024 for *hmF2*. We obtained the smallest PRMS for *foF2* deviation from the 'true' ionosonde's data 8.5% (GMF2, LSA) and 8.2% (GMF2cor, HSA) for the *foF2* model, and 9.5% (GMF2cor, LSA) and 4.7% (GMF2, HSA) for the *hmF2* model.

RMS between 'true' median *foF2obs* at 45 selected stations for 24 LT hours each month (Eq. 1) and the 'proxy' model *foF2* is shown in Fig. 9a, c (left panels). RMS between 'true' median *hmF2obs* and the 'proxy' *hmF2* is shown in Fig. 9b, d (right panels). The LSA (2019) data is in the lower panels and HSA (2024) data in the upper panel. Similar

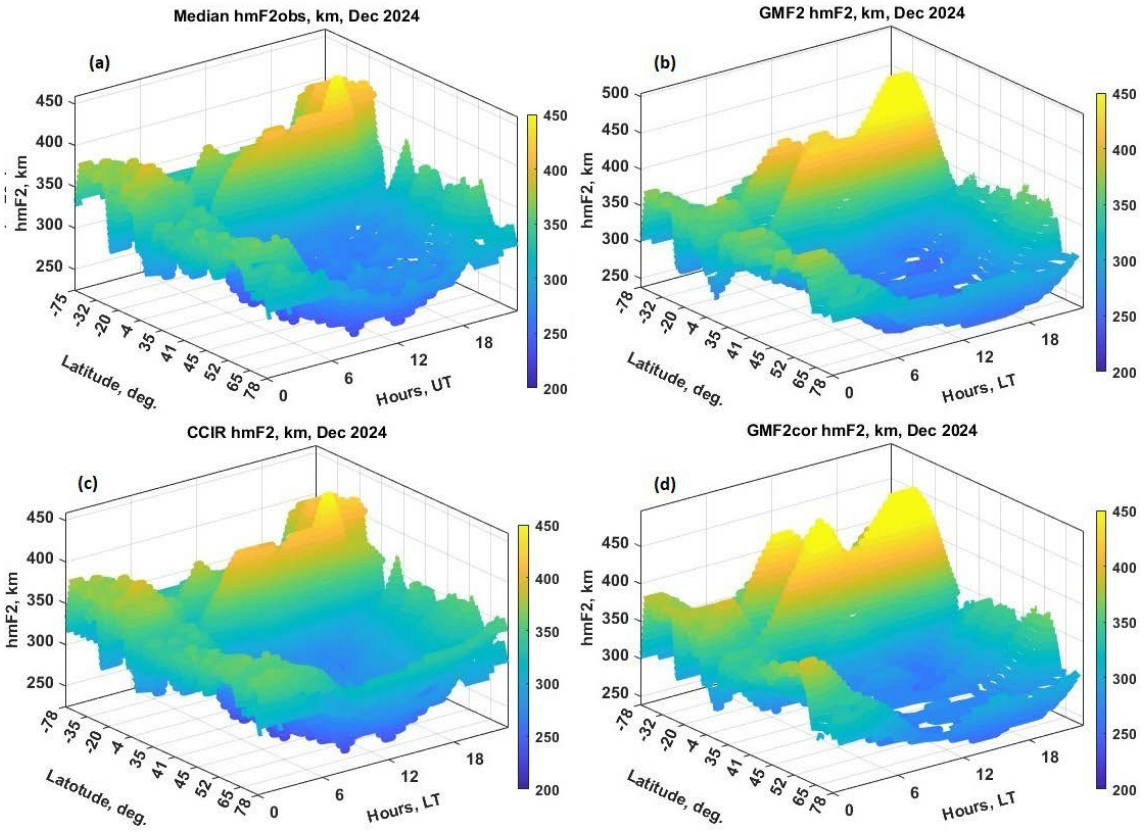

Figure 7. Diurnal – latitudinal variation of *hmF2* peak height: (a) observed median at 45 ionosonde stations; (b) GMF2 model; (c) *hmF2* model calculated from CCIR *M(3000)F2*; (d) GMF2 *hmF2cor* adapted to IRI-Plas foF2cor with GTEC model assimilation (Eq. 4).

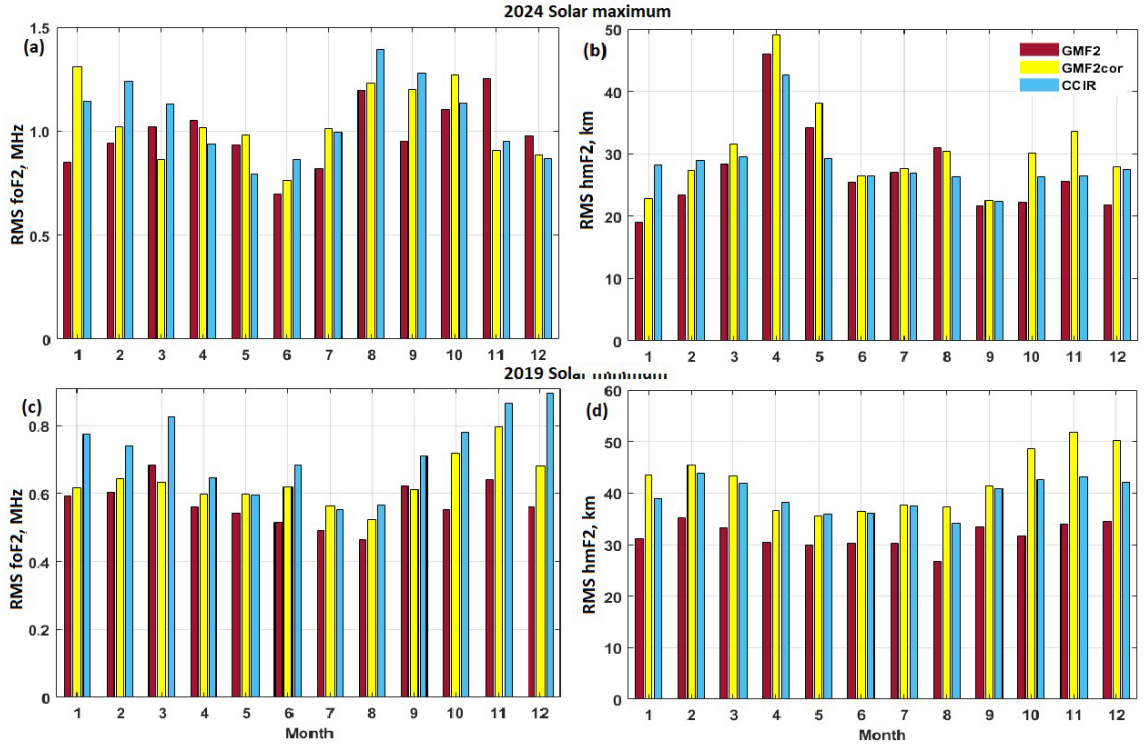

Figure 8. RMS for the 'truth' ~ 'model' data pairs for all months of 2019 (LSA) and 2024 (HSA) (GMF2 – red, GMF2cor – yellow and CCIR based results – cyan): (a) *foF2*, 2024; (b) *hmF2*, 2024; (c) *foF2*, 2019; (d) *hmF2*, 2019.

Table 1. PRMS (in percent, %) differences in the GMF2, GMF2cor and CCIR models from the 'true' monthly median *foF2* and *hmF2* of the ionosonde data.

HSA 2024	GMfoF2	GMfoF2cor	CCIRfoF2	GMhmF2	GMhmF2cor	CCIRhmF2
January	**9.6**	15.5	13.2	**4.7**	9.5	8.0
February	**9.3**	11.1	12.8	**6.0**	8.5	8.0
March	10.8	**8.2**	11.9	7.9	**7.6**	8.5
April	10.6	9.5	**8.6**	12.4	**11.6**	11.7
May	10.3	9.5	**8.5**	8.9	**7.5**	7.6
June	8.5	**8.3**	10.6	**6.3**	7.1	6.5
July	**8.8**	12.4	12.1	6.6	7.2	**6.4**
August	**10.5**	12.8	13.4	7.5	6.8	**6.2**
September	**8.8**	12.9	12.6	**5.3**	6.7	5.7
October	**10.1**	12.6	10.2	**5.3**	8.7	7.0
November	13.4	**9.4**	9.5	**6.3**	7.8	7.0
December	11.6	**10.4**	10.6	**5.4**	8.9	7.5
LSA 2019	**GMfoF2**	**GMfoF2cor**	**CCIRfoF2**	**GMhmF2**	**GMhmF2cor**	**CCIRhmF2**
January	**11.3**	13.2	15.7	**9.7**	15.0	12.9
February	**11.2**	12.7	14.1	**10.8**	15.2	14.4
March	**10.9**	11.6	14.8	**10.5**	14.1	13.7
April	**8.5**	10.5	10.3	**9.5**	11.9	12.3
May	**9.2**	11.7	10.1	**9.5**	11.8	11.7
June	**8.6**	12.6	12.6	**9.9**	12.2	12.1
July	**9.5**	11.7	10.7	**10.0**	13.1	12.9
August	**9.3**	11.4	10.7	**9.2**	13.1	12.2
September	**11.1**	12.2	12.8	**10.4**	13.8	14.0
October	**9.0**	12.8	13.6	**9.9**	16.6	14.5
November	**11.8**	14.9	16.4	**10.2**	18.0	14.1
December	**11.1**	13.4	17.3	**10.0**	17.0	11.2

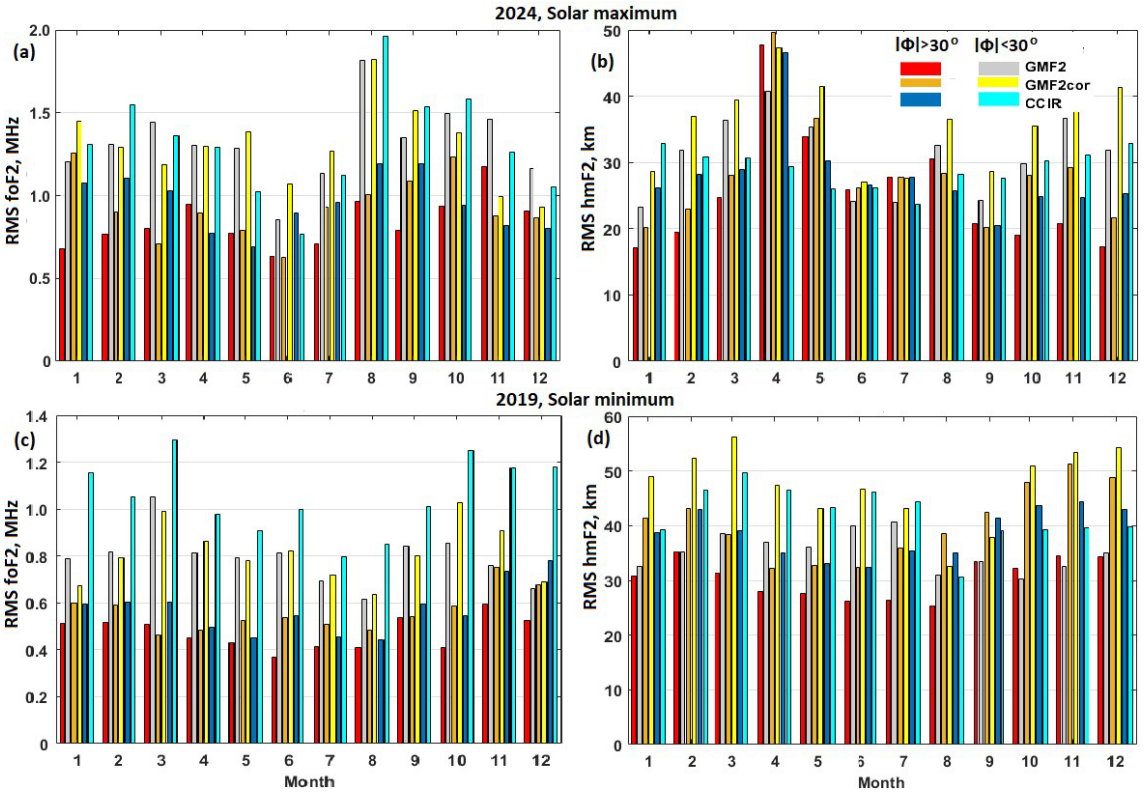

Figure 9. RMS for the ionosonde's 'true' ~ 'model' GMF2, GMF2cor and CCIR data pairs for all months of 2019 (LSA) and 2024 (HSA) for middle ($|\Phi| > 30°$) and low ($|\Phi| < 30°$) magnetic latitudes: (a) *foF2*, 2024; (b) *hmF2*, 2024; (c) *foF2*, 2019; (d) *hmF2*, 2019.

to global results in Fig. 8c, d, results of Fig. 9c, d show less RMS at GMF2 in all cases for LSA (2019). The results for HSA in Fig. 9a, b show few cases where CCIR results show less RMS for the F2 layer critical frequency and peak height. In particular, the advantage of CCIR results for foF2 in April and May 2024 and hmF2 in July and August 2024 is observed in both latitudinal regions. In most cases, we observe higher RMS values for low latitudes than for middle latitudes, which is associated with higher absolute values of observed *foF2* and *hmF2* in subequatorial regions, as seen in Figs. 6 and 7. Possible explanations for the discrepancies between the GMF2 and CCIR model results will be discussed in the next section.

4. Conclusions

CCIR maps of *foF2* and *M(3000)F2* are used in the International Reference Ionosphere, IRI, and IRI-Plas model to reproduce *foF2* critical frequency, peak height *hmF2*, 3D ionosphere spatial structure and total electron content, *TEC*. In this work, for the first time, we are implementing global 2D models – GMF2 of *foF2*, *hmF2* and GTEC maps – in conjunction with the IRI-Plas model for median prediction of *foF2m*, *hmF2m, Ne*(*h*)-profile, and *TECm* at altitudes between 65 km and 20000 km (GNSS orbit). IRI-Plas assimilation of *TEC* data to upgrade the F2 layer peak parameters is discussed in Eq. (3) and (4). Adjusting the *TEC* results obtained with IRI-Plas model using the F2 layer peak parameters *foF2* and *hmF2* from the GMF2 model to the global total electron content GTEC model yields a new set of adjusted IRI-Plas output parameters – *foF2cor, hmF2cor, Ne*(*h*)*cor* profile and *TECcor*.

We examined three implementations of IRI-Plas with the F2 layer peak parameters – CCIR, GMF2 and GMF2cor (aligned with GTEC model). First of all, we compare the IRI-Plas *TEC* results at different combinations of the F2 layer peak indices with measured 'true' data of UQRG GIM-TEC to assess reliability of the IRI-Plas *TEC* predictions. We obtain the RMS deviation of the different IRI-Plas options using CCIR and GMF2 maps from UQRG 'true' GIM-TEC data varying from 6.5 to 10.5 TECu which exceeds by about a factor of 2 the RMS of *TECmod* for GTEC model, varying from 4.6 to 7.0 TECu.

We then evaluate the sequence of CCIR, GMF2 and GMF2cor options in IRI-Plas using 'true' *foF2* and *hmF2* ionosonde data to assess their efficiency at low solar activity, LSA (2019) and high solar activity, HSA (2024) worldwide. The evaluation is carried out using data from 45 ionosondes located at different latitudes and longitudes so comparisons have been made between the characteristics of IRI-Plas with solar activity, latitude and local time. Overall, the GMF2 and GMF2cor results are found to be superior to the *foF2* and hmF2 CCIR model observed in RMS and percentage PRMS compared to the ionosonde observations. GMF2 more accurately captures the variation in *foF2* and *hmF2* in all months of low solar activity (2019) and in most cases high solar activity (2024).

The difference in specific months in the HSA is explained by differences in the source databases used in the construction of global models. While the CCIR model was constructed from ionosonde data for HSA (1957-1958) and LSA (1964), GMF2 models are based primarily on RO observation during 2001-2022 (75% foF2 and 92% hmF2), with the remaining data (25% foF2 and about 8% hmF2) of ionosonde observations during 1958-2022. Our comparisons here with ionosonde data suggest a difference between RO observations of F2 peak parameters and ionosonde measurements, in particular, during high solar activity, when different processes in the ionosphere are amplified. Thus, based on our results, we recommend the GMF2 *foF2* and *hmF2* to be default options in IRI and IRI-Plas models rather than the CCIR prediction.

We emphasize that the above results are obtained when comparing the monthly median 'model' ~ 'truth' data in accordance with the projectfor constructing the empirical models of IRI and IRI-Plas. To meet the demand for various operational goals, a step forward is the task of obtaining instant proxy *foF2* and *hmF2* using IRI-Plas adjustment of the median F2 layer peak parameters to the observed instant GIM-TEC. A detailed study of the simulation of the instant ionospheric state under quiet and perturbed conditions presents a challenge for a special investigation.

Data availability statement. UQRG GIM-TEC data can be downloaded at ftp://cddis.gsfc.nasa.gov/gps/products/ionex/, data GIRO at https://giro.uml.edu/didbase/scaled.php and the sunspot numbers at https://www.sidc.be/SILSO/home. IRI-Plas code is provided by IZMIRAN at https://www.izmiran.ru/ionosphere/weather/grif/SPIM/.

Acknowledgements. The authors thank Polytechnical University of Catalonia, Barcelona, Spain (UPC), gAGE/UPC, for UQRG GIM-TEC data. We acknowledge using data of the Global Ionospheric Radio Observatory (GIRO) at the University of Massachusetts, Lowell, USA, and the sunspot numbers at the Solar Influences Data Analysis Center, Brussells, Belgium. The authors are grateful to the two reviewers for their insightful and helpful comments.

References

Altadill, D., S. Magdaleno, J. M. Torta and E. Blanch (2013). Global empirical models of the density peak height and of the equivalent scaleheight for quiet conditions, Adv. Space Res., 52, 10, 1756-1769, doi:10.1016/j.asr.2012.11.018.

Arikan, F., U. Sezen and T. Gulyaeva (2019). Comparison of IRI-2016 F2 layer model parameters with ionosonde measurements, J. Geophys. Res. Space Phys., 124, 8092-8109, doi:10.1029/2019JA027048.

Bilitza, D., N. Sheik and R. Eyfrig (1979). A global model for the height of the F2-peak using M3000 values from the CCIR numerical map, Telecomm. J., 46, 549-553.

Bilitza, D. (2023). The International Reference Ionosphere – a model ionosphere, Eos, 104, doi:10.1029/2023EO235002.

Bilitza, D., D. Altadill, V. Truhlik, V. Shubin et al. (2017). International Reference Ionosphere 2016: from ionospheric climate to real-timeweather predictions, Space Weather, 15, 418-429, doi:10.1002/2016SW001593.

Bilitza, D., M. Pezzopane, V. Truhlik, D. Altadill et al. (2022). The International Reference Ionosphere model: a review and description of an ionospheric benchmark, Rev. Geophys., 60, e2022RG000792, doi:10.1029/2022RG000792.

Bilitza, D., V. Truhlik, Y. Omura and M. B. Moldwin (2024). Development and improvement of the International Reference Ionosphere with special emphasis on the topside and extension to the plasmasphere, Ann. Geophys., 67, 4, SA443, doi:10.4401/ag-9145.

CCIR Atlas of ionospheric characteristics (1966, 1975, 1991). ComitéConsultatif International des Radiocommunications, Report 340-1, 340-2, 340-6, International Telecommunication Union, Genève, Switzerland, ISBN:92-61-04417-4.

Edwards, D. J., T. E. Chambers and M. A. Cervera (2025a) CLIMF2: A climatological model of the ionospheric F2 layer. Part 1: Model methodology, Adv. Space Res., 75, 4143-4157, doi:10.1016/j.asr.2023.12.021.

Edwards, D. J., T. E. Chambers and M. A. Cervera (2025b) CLIMF2: A climatological model of the ionospheric F2 layer. Part 2: Validation and comparison with IRI, Adv. Space Res., 75, 4158-4174, doi:10.1016/j.asr.2023.12.002.

Galkin, I., A. Froń, B. Reinisch, M. Hernández-Pajares et al. (2022). Global monitoring of ionospheric weather by GIRO and GNSS data fusion, Atmosphere, 13, 371, doi:10.3390/atmos13030371.

Gerzen, T., D. Minkwitz and S. Schlueter (2015). Comparing different assimilation techniques for the ionospheric *F*2 layer reconstruction, J. Geophys. Res. Space Phys., 120, 6901-6913, doi:10.1002/2015JA021067.

Gulyaeva, T. (2012). Empirical model of ionospheric storm effects on the F2 layer peak height associated with changes of peak electron density, J. Geophys. Res. Space Phys., 117, A02302, doi:10.1029/2011JA017158.

Gulyaeva, T. L. and D. Bilitza (2012). Towards ISO standard earth ionosphere and plasmasphere model, in New Developments in the Standard Model R. J. Larsen (Ed.), 1-39, NOVA, Hauppauge, New York.

Gulyaeva, T. L., F. Arikan, M. Hernandez-Pajares and I. Stanislawska (2013). GIM-TEC adaptive ionospheric weather assessment and forecast system, J. Atmosph. Solar Terr. Phys., 102, 329-340, doi:10.1016/j.jastp.2013.306.011.

Hernández-Pajares, M., J. M. Juan, J. Sanz, R. Orus et al. (2009). The IGS-VTEC maps: a reliable source of ionospheric information since 1998, J. Geod., 83, 263-275, doi:10.1007/s00190-008-0266-1.

Hoque, M. M. and N. Jakowski (2011). A new global empirical NmF2 model for operational use in radio systems, Radio Sci., 46, RS6015, doi:10.1029/2011RS004807.

Hoque, M. M. and N. Jakowski (2012). A new global model for the ionospheric F2 peak height for radio wave propagation, Ann. Geophys., 30, 787-809, doi:10.5194/angeo-30-797-2012.

ISO 16457:2022 (2022). Space environment (natural and artificial) – The Earth's ionosphere model – International reference ionosphere (IRI) and extensions to the plasmasphere, ISO Standard, https://www.iso.org/standard/79476.html.

Jones, W. B. and R. M. Gallet (1962). The representation of diurnal and geographic variations of ionospheric data by numerical methods, Telecomm. J., 29, 129-149.

McNamara, L. F. and D. C. Thompson (2015). Validation of COSMIC values of foF2 and M(3000)F2 using ground-based ionosondes, Adv. Space Res., 55, 1, 163-169, doi:10.1016/j.asr.2014.07.015.

Paul, K. S., H. Haralambous, M. Moses and S. K. Panda (2025). Global accuracy assessment of ionospheric F2 peak characteristics based on coincident-colocated COSMIC-2 RO and Digisonde measurements: a three-year period analysis (2020-2022), Adv. Space Res., doi:10.1016/j.asr.2025.09.083.

Ratovsky, K. G., A. V. Dmitriev, A. V. Suvorova, A. A. Shcherbakov et al. (2017). Comparative study of COSMIC/FORMOSAT-3, Irkutsk incoherent scatter radar, Irkutsk Digisonde and IRI model electron density vertical profiles, Adv. Space Res., 60, 2, 452-460, doi:10.1016/j.asr.2016.12.026.

Roma-Dollase, D., M. Hernández-Pajares, A. Krankowski, K. Kotulak et al. (2017). Consistency of seven different GNSS global ionospheric mapping techniques during one solar cycle, J. Geod., 92, 691-706, doi:10.1007/s00190-017-1088-9.

Rush, C. M., M. Fox, D. Bilitza, K. Davies et al. (1989). Ionospheric mapping: An update of foF2 coefficients, Telecommun. J., 56, III, 179-182.

Shubin, V. N. (2015). Global median model of the F2-layer peak height based on ionospheric radio-occultation and ground-based digisonde observations, Adv. Space Res., 56, 916-928, doi:1016/j.asr.2015.05.029.

Shubin, V. N. (2017). Global empirical model of critical frequency of the ionospheric F2-layer for quiet geomagnetic conditions, Geomagn. Aeron., 57, 4, 414-425, doi:10.1134/S0016793217040181.

Shubin, V. N. and M. G. Deminov (2019). Global dynamic model of critical frequency of the ionospheric F2 layer, Geomagn. Aeron., 59, 4, 429-440, doi:10.1134/S0016793219040157.

Shubin, V. N. and T. L. Gulyaeva (2021). Solar forcing on the ionosphere: Global model of the F2 layer peak parameters driven by re-calibrated sunspot numbers, Acta Astronaut., 179, 197-208, doi:10.1016/j.actaastro.2020.10.029.

Shubin, V. N. and T. L. Gulyaeva (2022). Global mapping of Total Electron Content from GNSS observations for updating IRI-Plas model, Adv. Space Res., 69, 1, 168-175, doi:10.1016/j.asr.2021.09.032.

***CORRESPONDING AUTHOR: Tamara GULYAEVA**,
Pushkov Institute of Terrestrial Magnetism, Ionosphere and Radiowave Propagation, Russian Academy of Sciences, Moscow, Russia
e-mail: tam.gulyaeva@gmail.com